Electronic Supplementary Material (ESI) for Analytical Methods.

Electronic Supplementary Information

On-chip light sheet illumination for nanoparticle tracking in microfluidic channels

Théo Travers[1], Gaétan Delhaye[1], Martinus H. V. Werts [2], Denis Gindre[1], Matthieu Loumaigne[1,*]

[1]*Laboratoire MOLTECH-Anjou, UMR CNRS 6200, Univ Angers, SFR MATRIX, 2 Bd Lavoisier, 49000 Angers, France* [2]*Univ Rennes, CNRS, SATIE – UMR8029, F-35000 Rennes, France*

**E-mail: matthieu.loumaigne@univ-angers.fr*

Contents

1 Laser diode driver

Due to their exponential current-voltage characteristics, laser diodes require precise current control, which can be achieved using an LM317 voltage regulator configured as a current source, providing a straightforward and cost-effective solution. Although there may be more efficient current source alternatives, the simplicity and ease of implementation of the LM317-based circuit outweigh these considerations in the context of this study, making it a suitable choice for driving the laser diode.

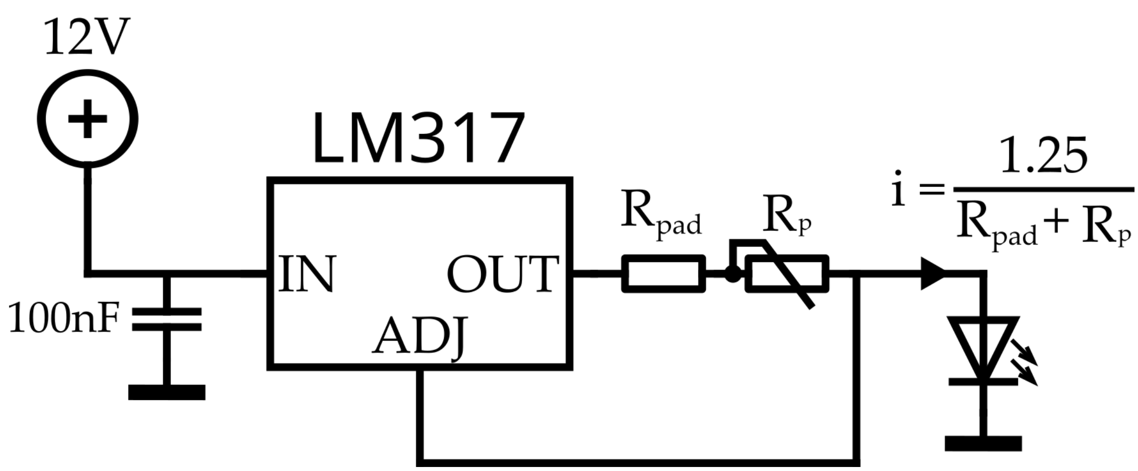

Figure 1 Schematic of the laser driver based on a LM317 regulator

The schematic of the laser driver is shown in figure 1. By design, the output current of LM317 is fixed at 1.25/R. R_{pad} set a maximum output current when the potentiometer is set at $R_p = 0\,\Omega$.

2 Optimization of fiber insertion

In the experimental phase involving the integration of optical fibers—either lens or laser fibers—into the microfluidic chip, precision and specific techniques are essential for successful implementation. The laser fiber's tip must be accurately positioned within the microchip's dry channel. This can be optimally achieved by utilizing a binocular microscope and stabilizing the laser fiber on a substrate that is level with the microchip's own substrate, followed by a controlled forward motion. For applications requiring a collimated light sheet, the laser fiber tip should be situated approximately at the back focal distance (BFD). However, in the case of focused light sheets, a higher degree of precision is mandated. The final micrometric adjustments are particularly challenging due to the friction encountered with the polydimethylsiloxane (PDMS) material. To mitigate the risk of fiber breakage within the microchip—a scenario that renders the device inoperable—it is advisable to minimize the length of the uncoated fiber segment to enhance its mechanical resilience.

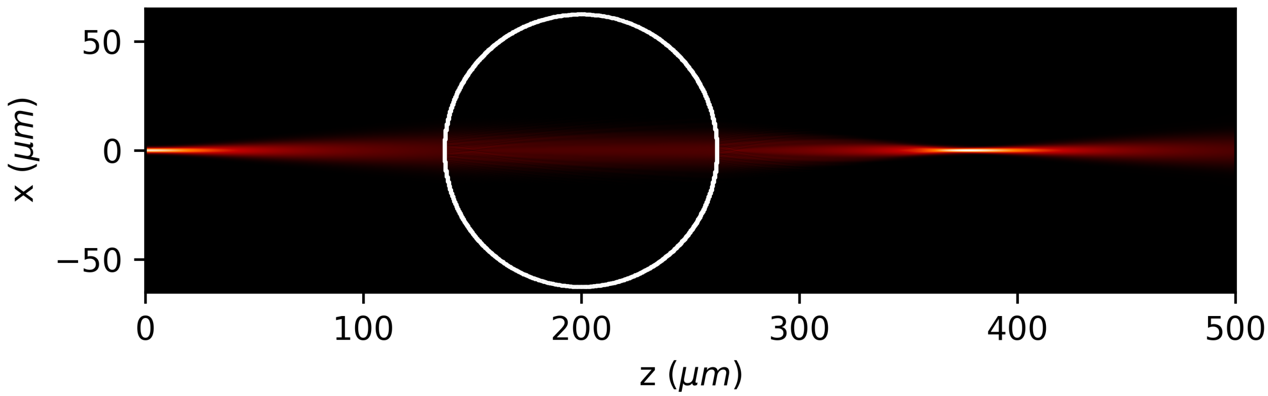

Figure 2 Numerical simulation obtained with diffractio[1] in the case of the focalization of a Gaussian beam by a step-index optical fiber modelized by two concentric spheres : the first one with radius $105/2$ and refractive index $n_{core} = 1.469$ and the second one with a radius of $125/2$ and a refractive index $n_{core} = 1.464$.

3 Effect of the step-index and gradient-index optical fiber on the focalization of a Gaussian beam

Fig. 2 presents the focalization profile of a Gaussian beam by a step-index optical fiber modelized by two concentric spheres the first one with radius $105/2$ microns and refractive index $n_{core} = 1.46958$ and the second one with a radius of $125/2$ microns and a refractive index $n_{core} = 1.46382$. No visible effects are apparent at the boundary of the cladding and the core of the optical fiber and no difference was seen in the case with just one sphere with a constant refractive index.

4 Ray transfer matrix of a ball lens

The ray transfer matrix of a thick lens can be seen as the succession of a concave spherical interface with a radius of curvature R_1 separating a medium of refractive index n_1 and the lens of refractive index n_2 followed by a length d of free propagation and finally a convex spherical surface with a radius of curvature R_2 separating the lens from a medium of refractive index n_3. Thus, it can be written as [2] :

$$M_{\text{thick lens}} = \begin{pmatrix} 1 & 0 \\ \frac{1}{R_2}\left(1-\frac{n_2}{n_3}\right) & \frac{n_2}{n_3} \end{pmatrix} \begin{pmatrix} 1 & d \\ 0 & 1 \end{pmatrix} \begin{pmatrix} 1 & 0 \\ -\frac{1}{R_1}\left(1-\frac{n_1}{n_2}\right) & \frac{n_1}{n_2} \end{pmatrix} \tag{1}$$

A ball lens is a special case where the two radii of curvature are the same ($R_1 = R_2 = R$) and the distance d between the two spherical interfaces is equal to the diameter $D = 2R$ of the sphere. Consequently,

$$M_{\text{ball lens}} = \begin{pmatrix} -1+2\frac{n_1}{n_2} & 2R\frac{n_1}{n_2} \\ -\frac{n_1n_2-2n_1n_3+n_2n_3}{n_2n_3R} & n_1\left(\frac{2}{n_2}-\frac{1}{n_3}\right) \end{pmatrix} \tag{2}$$

The image focal distance f_{image} can be obtained by calculating where a ray parallel to the optical axis crosses the optical axis after going through the lens. The incoming ray has for vector :

$$v_{\text{in}} = \begin{pmatrix} x = 1 \\ \theta = 0 \end{pmatrix} \tag{3}$$

where x is the distance from the optical axis and θ is the angle with the optical axis. The light ray exiting the ball lens has for vector :

$$v_{\text{out}} = M_{\text{ball lens}} \cdot v_{\text{in}} = \begin{pmatrix} x_{\text{out}} \\ \theta_{\text{out}} \end{pmatrix} = \begin{pmatrix} -1+2\frac{n_1}{n_2} \\ -\frac{n_1n_2-2n_1n_3+n_2n_3}{n_2n_3R} \end{pmatrix} \tag{4}$$

and crosses the optical axis at distance $x_{\text{out}}/\theta_{\text{out}}$ from the right side of the ball lens (where we assume that $\tan\theta_{\text{out}} \approx \theta_{\text{out}}$ as usual for paraxial rays). Subtracting R in order to obtain the distance from the center of the ball lens, we obtain[1] :

$$f_{\text{image}} = \frac{-n_1n_2R}{n_1(n_2-2n_3)+n_2n_3} \tag{5}$$

When the ball lens is immersed in air, $n_1 = n_2 = 1$ and the image focal distance drops back to $f_{\text{image}} = -nD/(4(n-1))$ as in the standard textbook [2].

As for the object focal distance, it can be found by firstly calculating an input light ray that would give an output ray parallel to the optical axis (with $\theta_{\text{out}} = 0$) and then calculating the position where the input ray crosses the optical axis.

$$v_{\text{in}} = (M_{\text{ball lens}})^{-1} \cdot v_{\text{out}} = \begin{pmatrix} x_{\text{in}} \\ \theta_{\text{in}} \end{pmatrix} = \begin{pmatrix} \left(\frac{2}{n_2}-\frac{1}{n_3}\right) \\ -\frac{n_1n_2-2n_1n_3+n_2n_3}{n_1n_2R} \end{pmatrix} \tag{6}$$

[1] Equivalently, we can directly use the formula $f_{\text{image}} = A/C$ where A and C are the ABCD coefficient matrix of the ball lens (cf eq.2)

and crosses the optical axis at distance $x_{\text{in}}/\theta_{\text{in}}$. Adding R to this distance give the object focal distance f_{object}[2] :

$$f_{\text{object}} = \frac{n_2 n_3 R}{n_1(n_2 - 2n_3) + n_2 n_3} \tag{7}$$

Once again, this distance reverts to $nD/(4(n-1))$ in the case where $n_1 = n_2 = 1$.

If the first part of the ball lens is in the air ($n_1 = 1$) and the second part is surrounded by PDMS ($n_3 = n_{\text{P}}$) and if we note the index of refraction of the lens $n_2 = n$, we obtain :

$$f_{\text{image}} = \frac{-nR}{n - 2n_{\text{P}} + nn_{\text{P}}} \quad \text{and} \quad f_{\text{object}} = \frac{nn_{\text{P}} R}{n - 2n_{\text{P}} + nn_{\text{P}}} \tag{8}$$

In the same conditions, the ABCD matrix is given by :

$$M_{\text{ball lens}} = \begin{pmatrix} -1 + \frac{2}{n} & \frac{2R}{n} \\ -\frac{n - 2n_P + nn_P}{nn_P R} & \frac{2}{n} - \frac{1}{n_P} \end{pmatrix} \tag{9}$$

[2]Equivalently, we can directly use the formula $f_{\text{object}} = -D/C$ where D and C are the ABCD coefficient matrix of the ball lens (cf eq.2

5 Propagation of a Gaussian beam through the optical system

The optical system is schematized in figure 3.

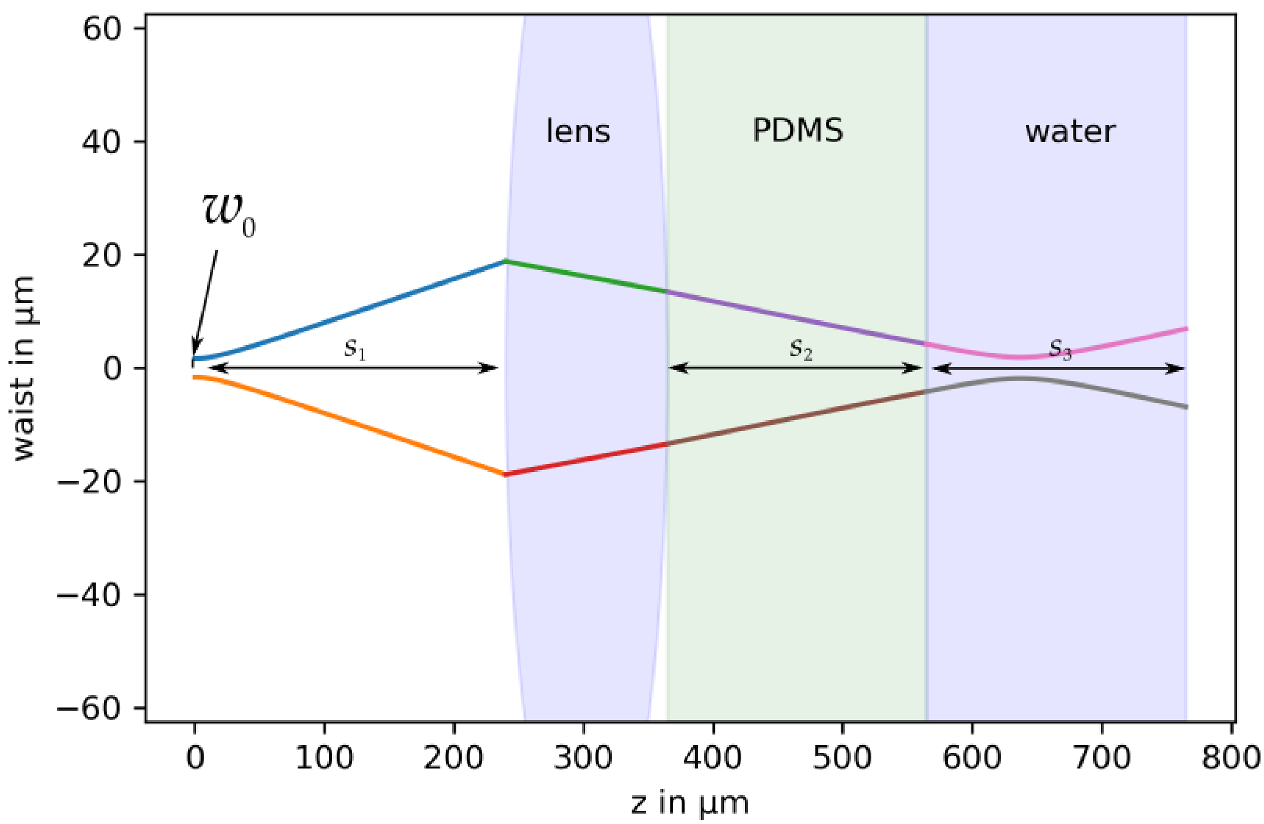

Figure 3 Optic schematics for the calculation of the Gaussian beam through the different media. The diameter of the ball lens is fixed at $125\,\mu$m.

The beam exiting the single mode fiber can be approximated by a Gaussian beam with a waist w_0 equal to half the diameter of the mode field (here $3.3\,\mu$m, hence $w_0 = 1.75\,\mu$m and an infinite radius of curvature $R(z)$. This beam can be represented by a complex number q with $1/q = -i\lambda/(\pi n w(z)^2) + 1/R(z)$ where λ is the wavelength of the light (here $\lambda = 405\,$nm, z is the optical axis coordinate, $w(z)$ is the waist of the Gaussian beam at position z and $R(z)$ its radius of curvature and n is the refractive index of the medium of propagation [3]).

The waist at the propagation position z can be obtained through the complex parameter $q(z)$ by :

$$w(z) = \frac{\lambda}{n\pi\Im(q)}|q|^2 \tag{10}$$

where $\Im(q)$ is the imaginary part of q

At the exit of the optical fiber, where the radius of curvature $R(z)$ is infinite, the complex parameter of the Gaussian beam q is purely imaginary and equals :

$$q_{\text{fiber}} = i\frac{\pi w_0^2}{\lambda} = iz_r \tag{11}$$

where $z_r = \pi w_0^2/\lambda$ is the Rayleigh range.

Using ABCD ray transfer matrix, one can calculate the evolution of the complex parameter q of the beam through the propagation of the different optics[3].

More precisely, the input complex parameter q is transformed in q' after propagating through an optic represented by a ABCD matrix via[4] [3] :

$$q' = \frac{Aq+B}{Cq+D} \tag{13}$$

Propagation from the fiber over the distance s_1 to the ball lens in the air leads to the complex parameter q_1 :

$$q_1 = q_{\text{fiber}} + s_1 = iz_r + s_1 \tag{14}$$

The ball lens transform q_1 in q_2 via

$$q_2 = \frac{Aq_1+B}{Cq_1+D} \tag{15}$$

with the ABCD coefficient obtained from equation 9. Thus, we can write :

$$q_2 = \frac{BD + (BC+AD+ACs_1)s_1 + ACz_r^2}{(Cs_1+D)^2 + C^2z_r^2} + i\frac{-z_r(BC+AD)}{(Cs_1+D)^2+C^2z_r^2} \tag{16}$$

Propagation in PDMS from the lens to the fluid distanced by s_2, microchannel transforms q_2 in q_3 with:

$$q_3 = q_2 + s_2 \tag{17}$$

The refraction between the PDMS and the water at the microchannel interface transforms q_3 in q_4 via[5] :

$$q_4 = \frac{n_w}{n_P} q_3 \tag{18}$$

where $n_w = 1.33$ is the refractive index of water.

Finally, the beam propagates in the water (distance s_3 where it may focalize. It transforms from q_4 to q_5 with :

$$q_5 = q_4 + s_3 \tag{19}$$

Alternatively, one can also form a single matrix for the overall optical system :

$$M_{\text{sys}} = \begin{pmatrix} 1 & s_1 \\ 0 & 1 \end{pmatrix} \begin{pmatrix} A & B \\ C & D \end{pmatrix} \begin{pmatrix} 1 & s_2 \\ 0 & 1 \end{pmatrix} \begin{pmatrix} 1 & 0 \\ 0 & \frac{n_P}{n_W} \end{pmatrix} \begin{pmatrix} 1 & s_3 \\ 0 & 1 \end{pmatrix} \tag{20}$$

[3]Only the coefficient A and B will affect the waist of the propagating Gaussian beam through the optical system described by an ABCD matrix. More precisely, the input waist w is transformed into the exit waist w' via :

$$w' = w\sqrt{\left(\frac{\lambda B}{\pi w^2}\right)^2 + \left(A + \frac{B}{R^2}\right)^2} \tag{12}$$

We can see that if $B = 0$ and $A = 1$ then the waist will be unchanged by the optics

[4]if one wants to trace the beam through the ball lens, like in section 4, then the full ABCD matrix of the ball lens (eq.2) has to be broken into its three parts like in equation 1.

[5]The ABCD matrix of refraction at a flat surface from refractive index n_1 to n_2 is :

$$\begin{pmatrix} 1 & 0 \\ 0 & \frac{n_1}{n_2} \end{pmatrix}$$

The focal spot position z_f is reached when the radius of the beam curvature is infinite and when the complex parameter q is purely imaginary. This happens when the distance s_3 is equal to :

$$-\frac{n_W}{n_P}\left(\frac{BD+(BC+AD+ACs_1)s_1+ACz_r^2}{(Cs_1+D)^2+C^2z_r^2}+s_2\right) \tag{21}$$

In practice, it is maybe easier to use a numerical approach than using a literal formula like eq.21.

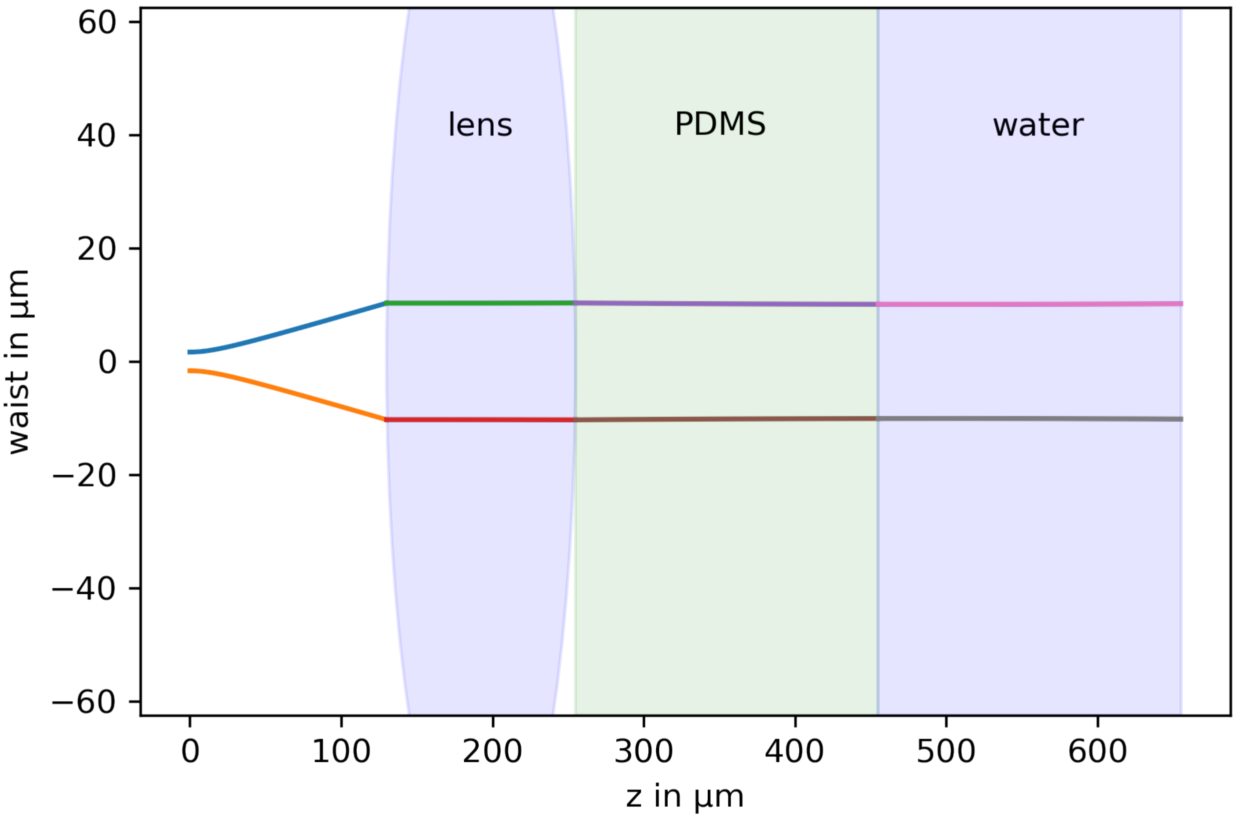

Figure 4 Gaussian beam propagation obtained with paraxial Ray transfer matrix calculation in the case of a collimating beam ($s_1 = 130\mu$m)

6 Ray tracing of a Gaussian beam in the paraxial approximation

Based on the mathematical development presented in the previous SI sections Python scripts were written to calculate the propagation of a Gaussian across the optical system using Ray transfer matrix. These scripts can be found at `https://github.com/MLoum/On-chip-light-sheet-illumination-for-nanoparticle`

Figures 4, 5 and 6 presents obtained with the mentioned Python script for different optics configuration, namely collimated (fig. 4), slightly converging (fig. 5) and strongly converging (fig. 6). Figures 7, presents the case where there is no cylindrical lens.

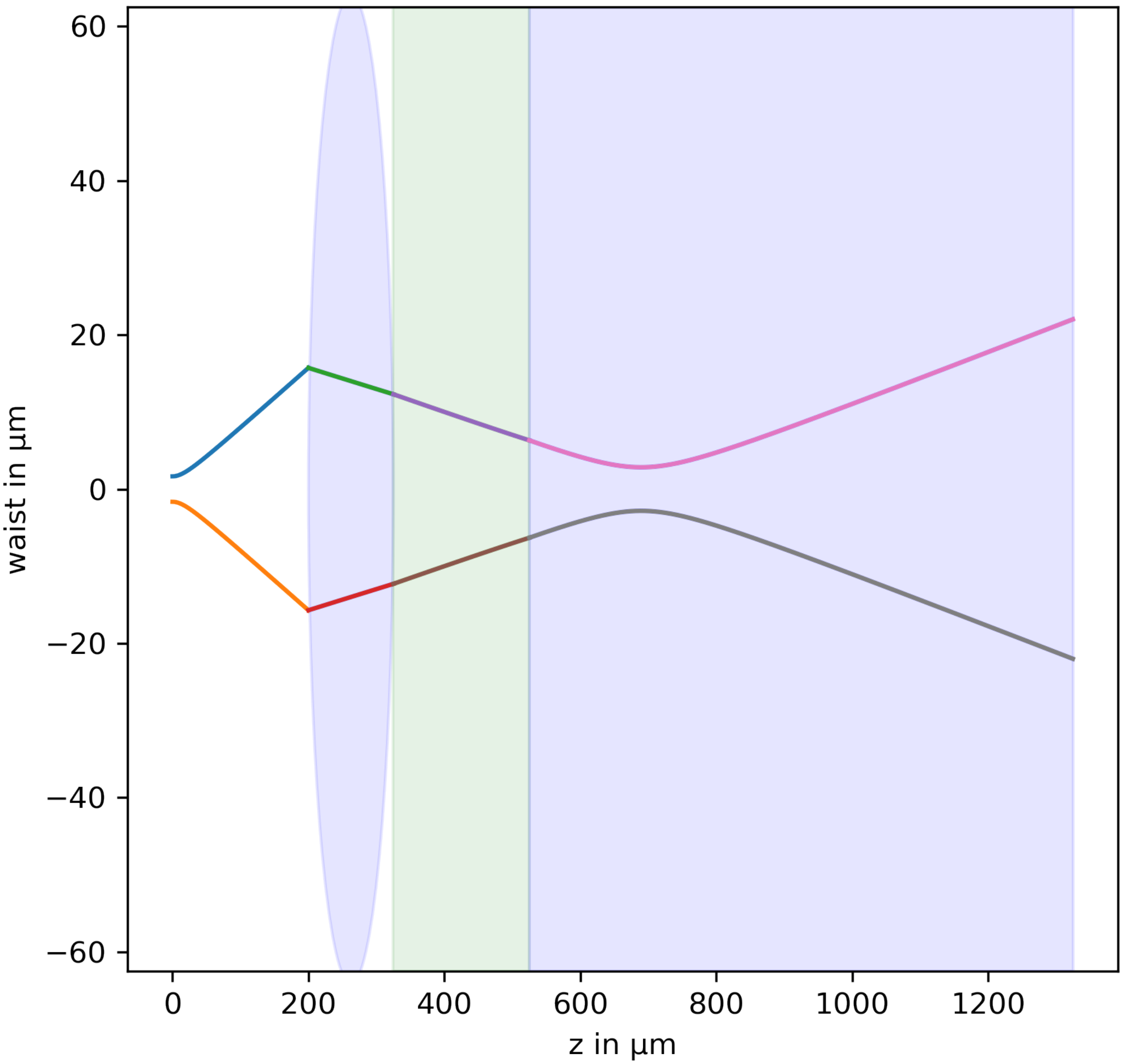

Figure 5 Gaussian beam propagation obtained with paraxial Ray transfer matrix calculation in the case of a slightly convergent beam ($s_1 = 150\mu$m).

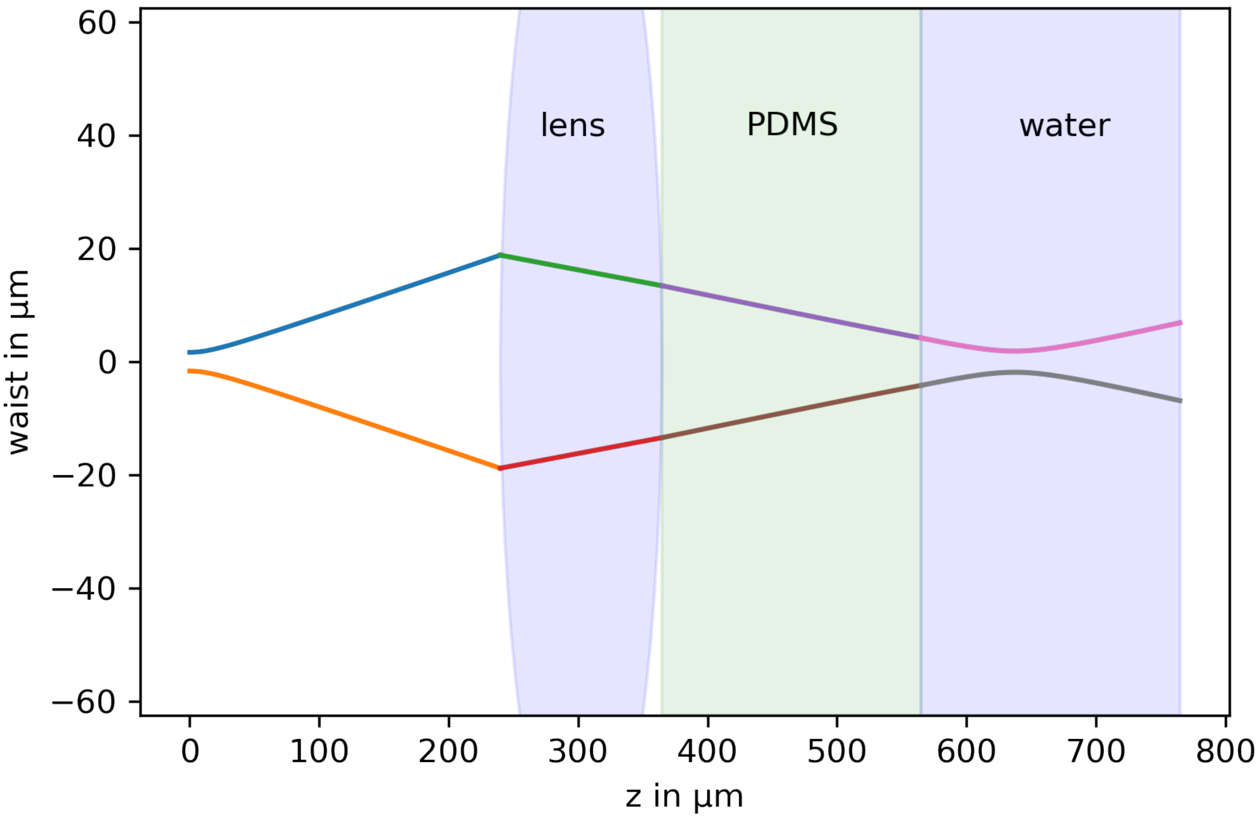

Figure 6 Gaussian beam propagation obtained with paraxial Ray transfer matrix calculation in the case of a strongly convergent beam ($s_1 = 240 \mu\mathrm{m}$).

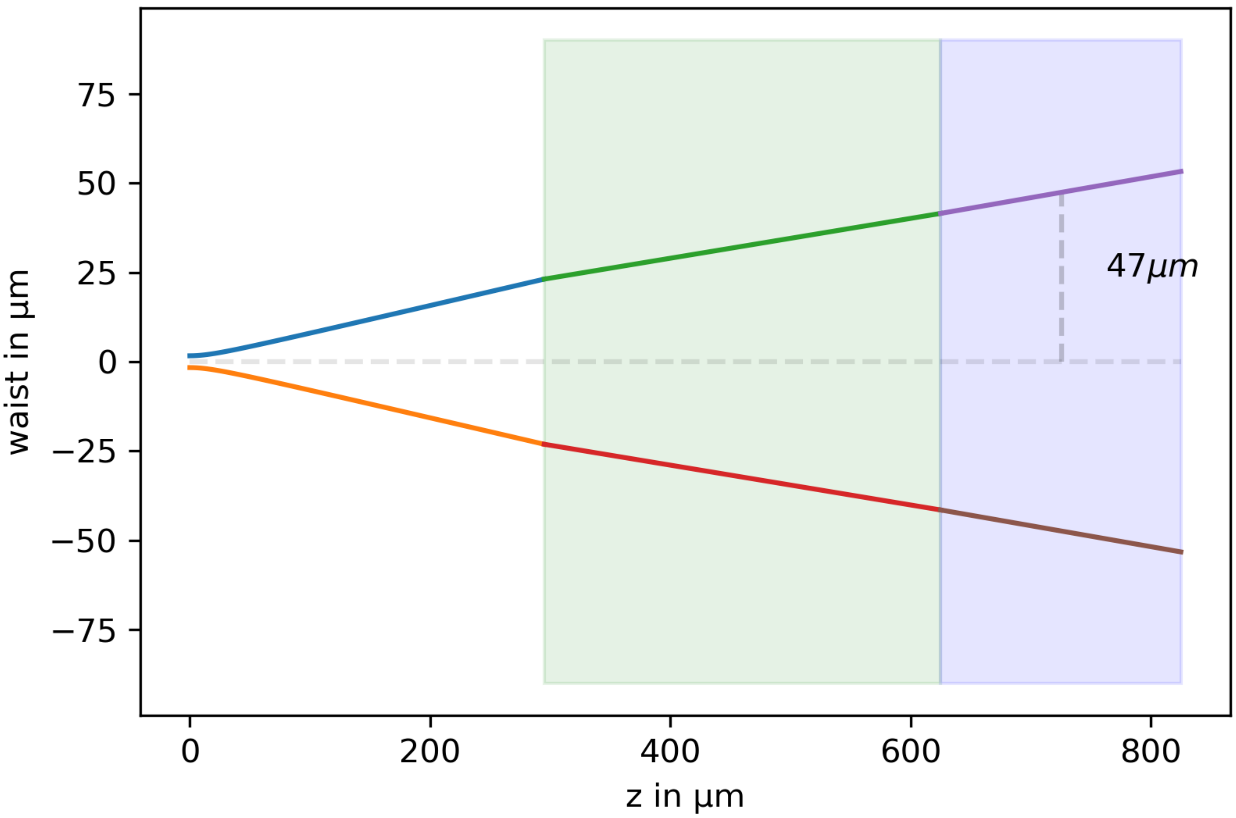

Figure 7 Gaussian beam propagation obtained with paraxial Ray transfer matrix calculation when there is no lens but only diopters ($s_1 = 300\mu\text{m},\ s_3 = 100\mu\text{m}$).

7 Evolution of the waist and Rayleigh length with the position of the optical fiber

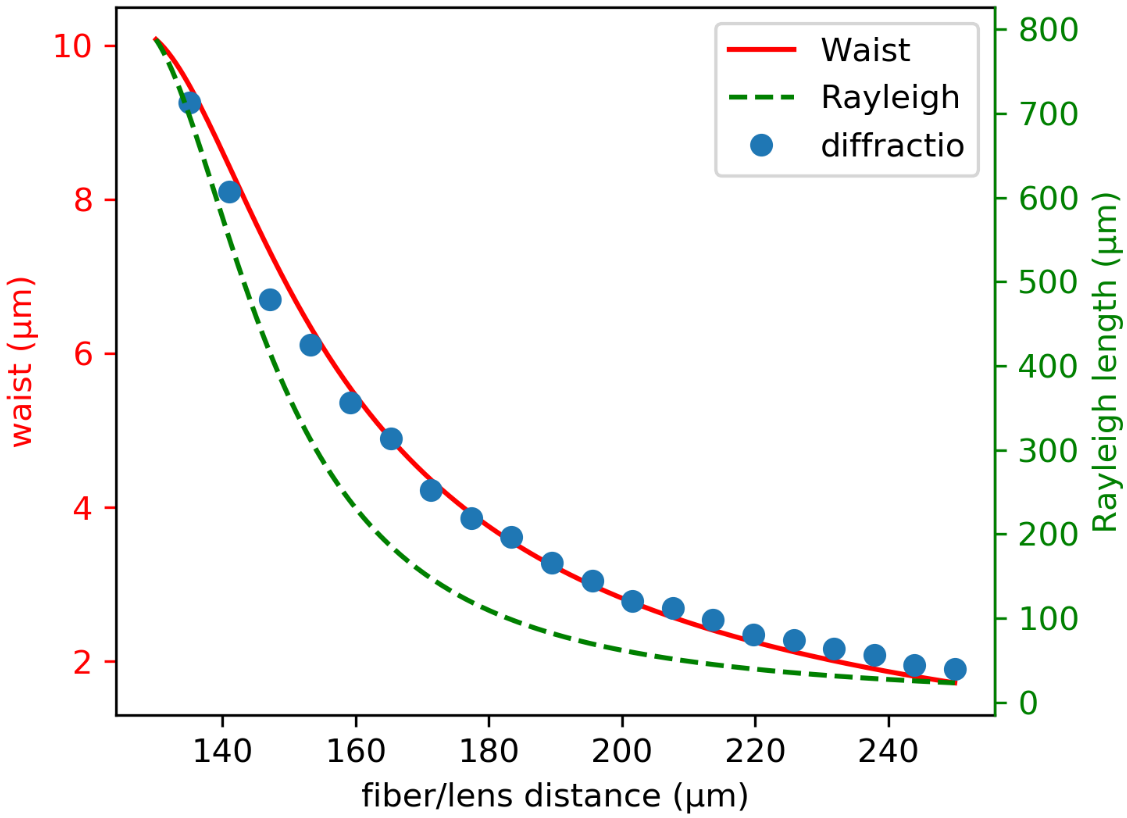

Figure 8 Evolution of the waist and Rayleigh length with the distance between the optical fiber and the boundary of the cylindrical lens (and not its center) in the case where the cylindrical lens is in contact with PDMS. The plain line was obtained with ray transfer matrix calculation whereas the point where obtained used numerical simulation with diffractio.

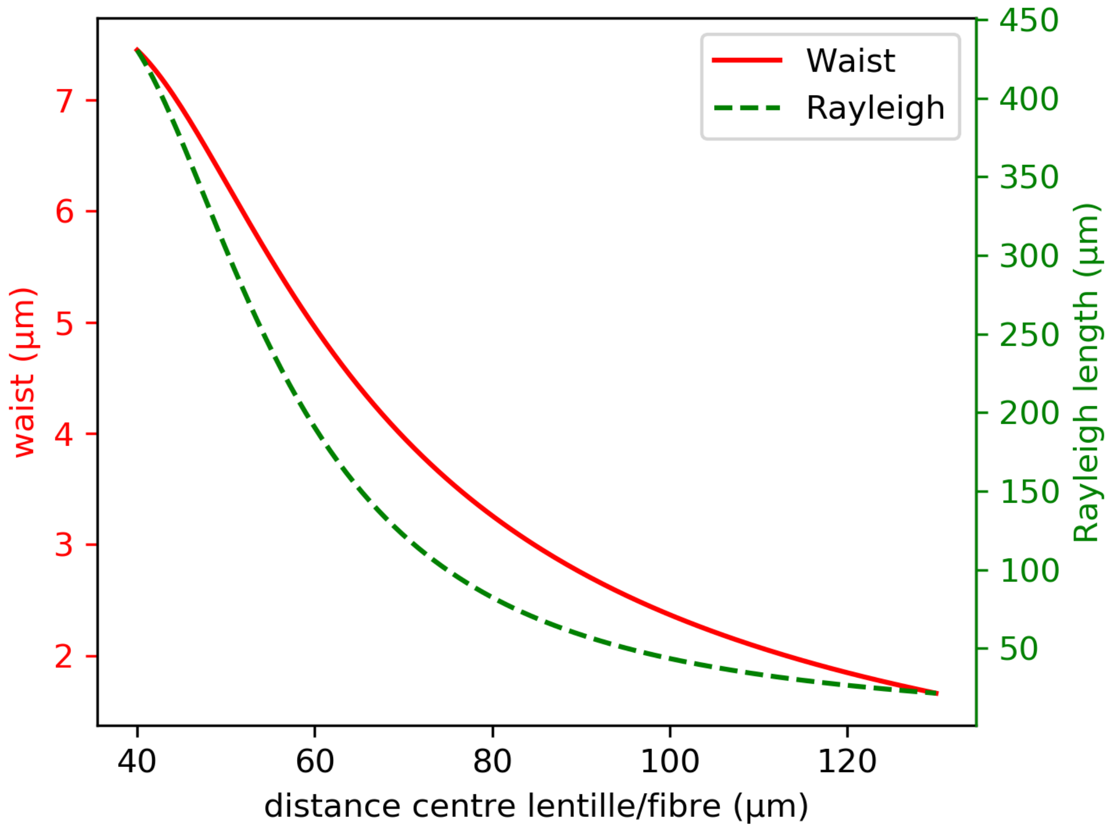

Figure 9 Evolution of the waist and Rayleigh length with the distance between the optical fiber and the boundary of the cylindrical lens (and not its center) in the case where the cylindrical lens is not in contact with PDMS.

8 Gaussian beam parameters

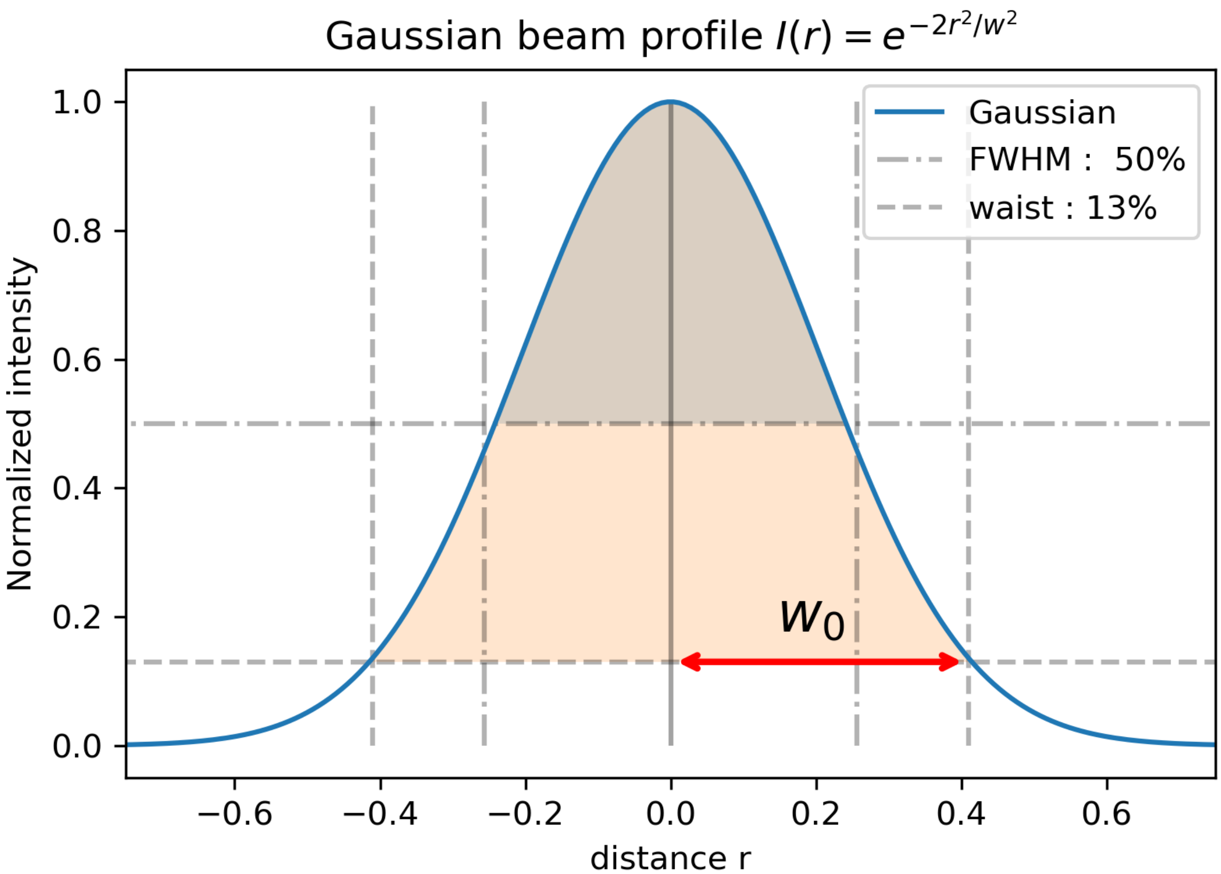

Figure 10 Radial profile of the intensity of a Gaussian at a given z position along the optical axis. The waist w_0 is the *radius* of the distance from the center of the beam where the maximum intensity is divided by e^2, that is to say 13%.

The intensity of a Gaussian beam is derived from the square of the electric field distribution, and it forms a Gaussian profile in the transverse plane perpendicular to the direction of propagation. This distribution can be written as (see fig 10):

$$I(r,z) = I_0 \left(\frac{w_0}{w(z)} \right)^2 e^{-2r^2/w^2(z)} \tag{22}$$

In this equation, I_0 is the peak intensity at the center of the beam waist, w_0 is the waist size, $w(z)$ is the radius at which the field amplitude and intensity are reduced to $1/e$ and $1/e^2$ (that is to say 13%) of their axial values, respectively, and r is the radial distance from the beam axis.

The waist $w(z)$ of the beam evolves along the propagation axis z according to the formula (see fig 11) :

$$w(z) = w_0 \sqrt{1 + \left(\frac{z}{z_R} \right)^2} \tag{23}$$

Here, z_R is the Rayleigh range, defined as:

$$z_R = \frac{\pi w_0^2}{\lambda} \tag{24}$$

where λ is the wavelength of the light. The waist w_0 and Rayleigh range z_R are crucial parameters that completely describe the beam and its evolution along the propagation axis. The waist size $w(z)$ reaches its minimum, w_0, at $z = 0$ and increases for $|z| > 0$, illustrating the beam's divergence away from the focus. At the Rayleigh length z_R the beam waist is $w(z_R) = \sqrt{2}w_0$.

The Full Width at Half Maximum (FWHM) of the intensity profile at the beam waist is related to the waist size by:

$$\mathrm{FWHM} = 2\sqrt{2\ln 2}w_0 \approx 1.1774w_0 \tag{25}$$

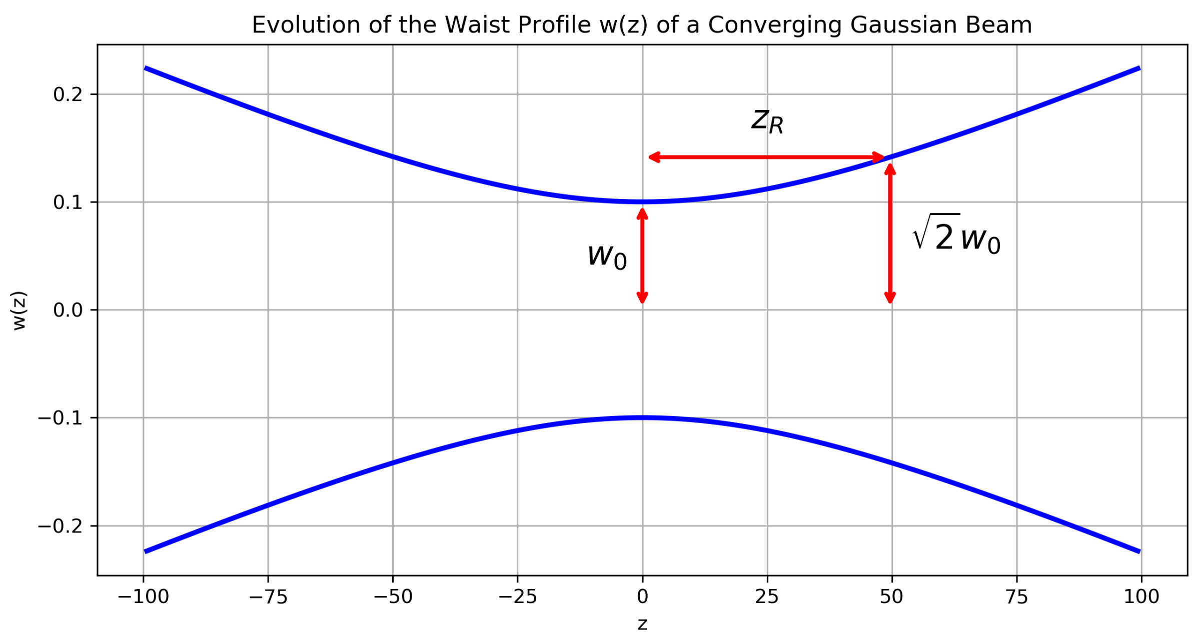

Figure 11 Schematic of the profile $w(z)$ of a focalizing Gaussian beam that front cases the definition of the w_0, that is to say the minimum waist size at the focal point, and the Rayleigh length $z_r = \pi w_0^2/\lambda$, that is to say, the distance from the focal point where the waist is $w(z_R) = \sqrt{2}w_0$

9 Depth of field determination

The depth of the light sheet can change along the width of the channel. For the collimated option, it can appear due to a miss positioning of the fiber around the focal point but it barely affects the thickness as figure 12 shows for three different positions. However, for the focused light sheet, inherently to the beam waist proprieties, the light sheet thickens depending on the distance to the center of the waist.

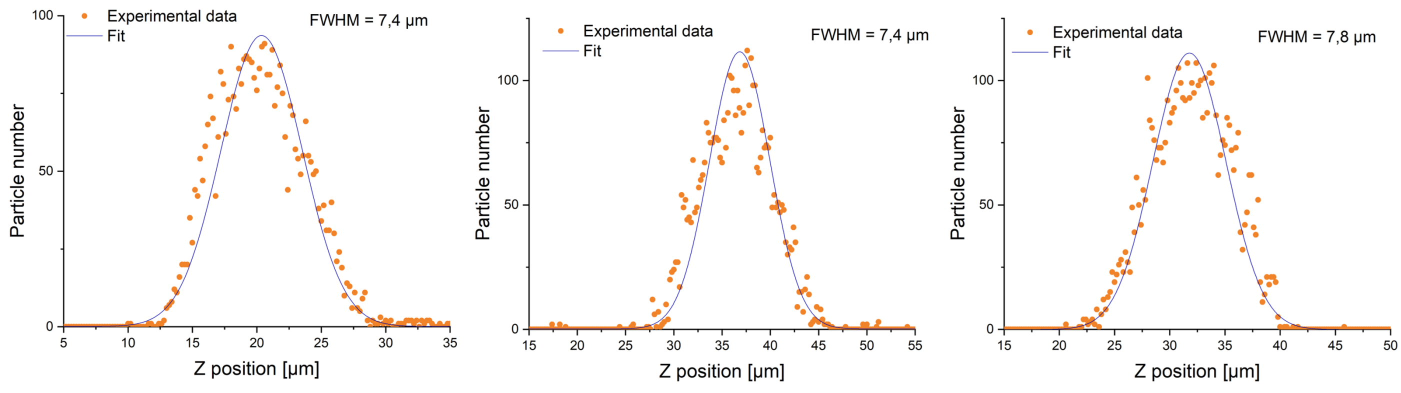

Figure 12 Estimated light-sheet size with the Z-stack method for different positions between the lens and the fiber. On the right 145μm, On the middle 110μm and on the left 90μm.

For particle tracking, we established a different definition of the depth of field (DOF) taking into account the maximal distance were a particle can be detected from the background noise. Because the diffraction pattern of an out of focus bead is an airy disk, a simulation can estimate the intensity axial profile of the beads when it goes away from the focal plane. Figure 13 shows the axial evolution of the central pixels intensity in the diffraction pattern. To generate the theoretical pattern, the scalar-based diffraction model of Gibson & Lanni is used with the plugin "PSF generator" of Fiji [4].

10 Light-sheet lateral profile

The article mainly deals with the axial profile of the light sheet which is the one that is focused by the cylindrical lens and is the one increasing the signal-to-noise ratio for single particle tracking.

However, the cylindrical lens does not affect the lateral evolution of the light sheet. Consequently, the beam exiting the optical fiber is diverging with a half angle related to the numerical aperture of the optical fiber namely 0.12. Taking into account the refraction at the air/PDMS boundary and then the PDMS/water boundary, the calculated lateral half angle divergence of the should be around $4.6°$. This is confirmed experimentally as shown in figure 14 by creating the light sheet with a micro-channel filled with a fluorophore (Atto 390) and imaging the corresponding fluorescence on the camera.

Hence, the lateral size of the light sheet where the tracking can be performed is dependent of the distance between the optical fiber and the micro-channel. However, this distance also determines the light sheet thickness and homogeneity. Consequently, a compromise has to be found. For instance, in Fig. 14, only a part of the field of view of the microscope is lightened with the light sheet. Placing the microchannel further away from the optical fiber would have enlarged the zone of study, but at the same time, it would have changed the light-sheet thickness and its axial homogeneity.

Refractive index immersion n_i	1
Refractive index sample n_s	1,33
Working distance t_i [µm]	610
Wavelength [nm]	405
Pixel size XY [nm]	263
Numerical aperture	0,75
Z-setp [nm]	25
Image dynamic range	8-bits

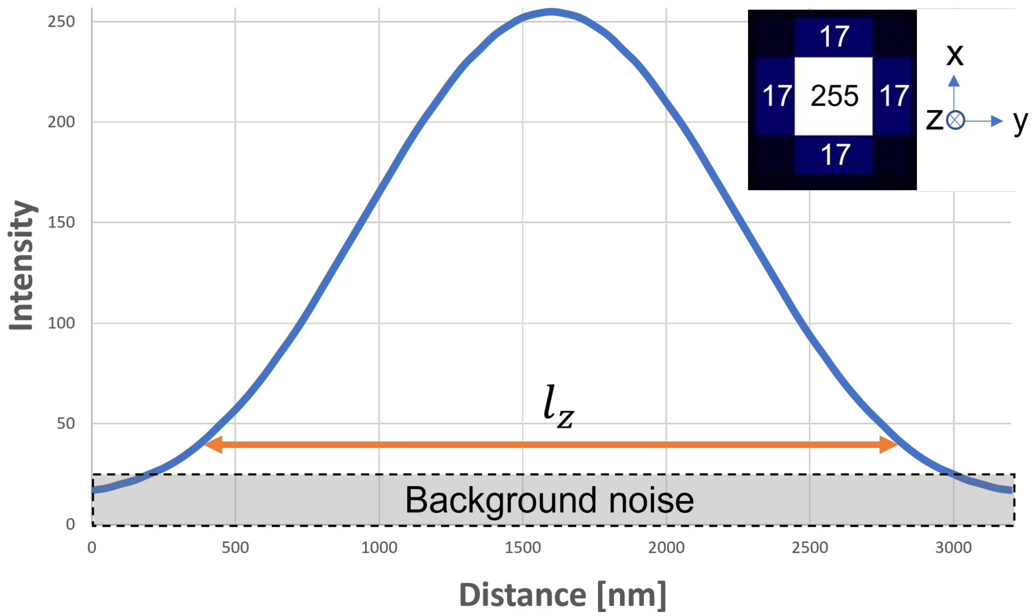

Figure 13 : Simulation of the PSF intensity profile along Z axis to approximate the axial volume length l_z where a particle can be discerned from background noise. Left panel shows the input parameters and the right curve is the Z axis intensity profile from the central part of the PSF (4 pixels). The choice of resolution was made to fits with the experiment. The upper right corner shows the pattern of the PSF and the value of each pixel describes the XY intensity profile. PSF generator, Daniel Sage and Hagai Kirshner, Biomedical Imaging Group (BIG) EPFL, Lausanne, Switzerland.

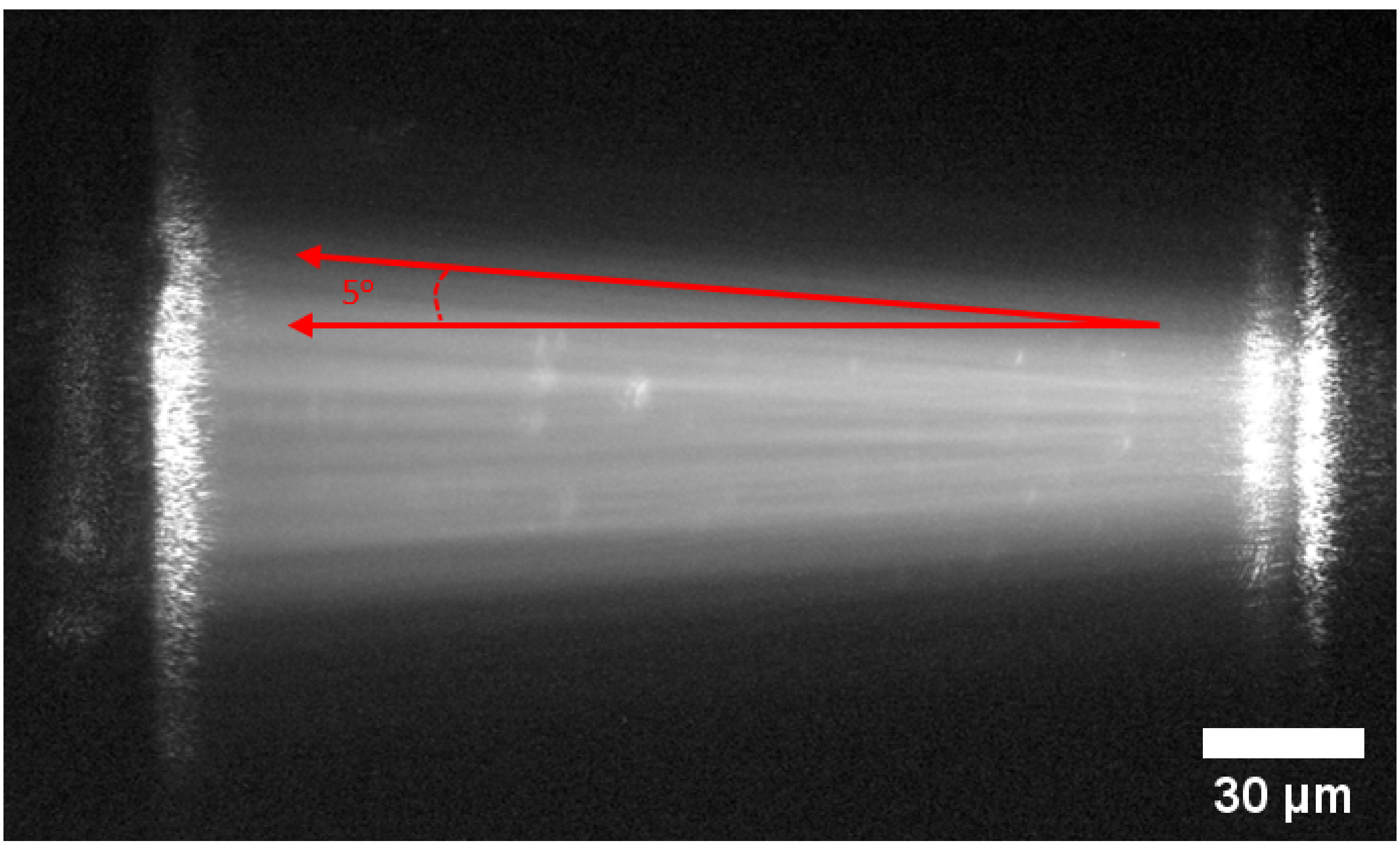

Figure 14 Image of the fluorescence of Atto 390 excited with a light sheet. The estimated divergence (around 5°) is compatible with the calculated one. The microdevice is the one described in Fig2.B, that is to say with a cylindrical lens but without an air notch.

11 TrackMate detection procedure

The TrackMate detection procedure needs to be optimized to adapt the algorithm input. Knowing that the size of the particles influences their velocity, the search radius from the particle position to the next one is a crucial parameter. The whole detection process is described in the SI of the work on "Single-Particle Tracking with Scanning Non-Linear Microscopy"[5].

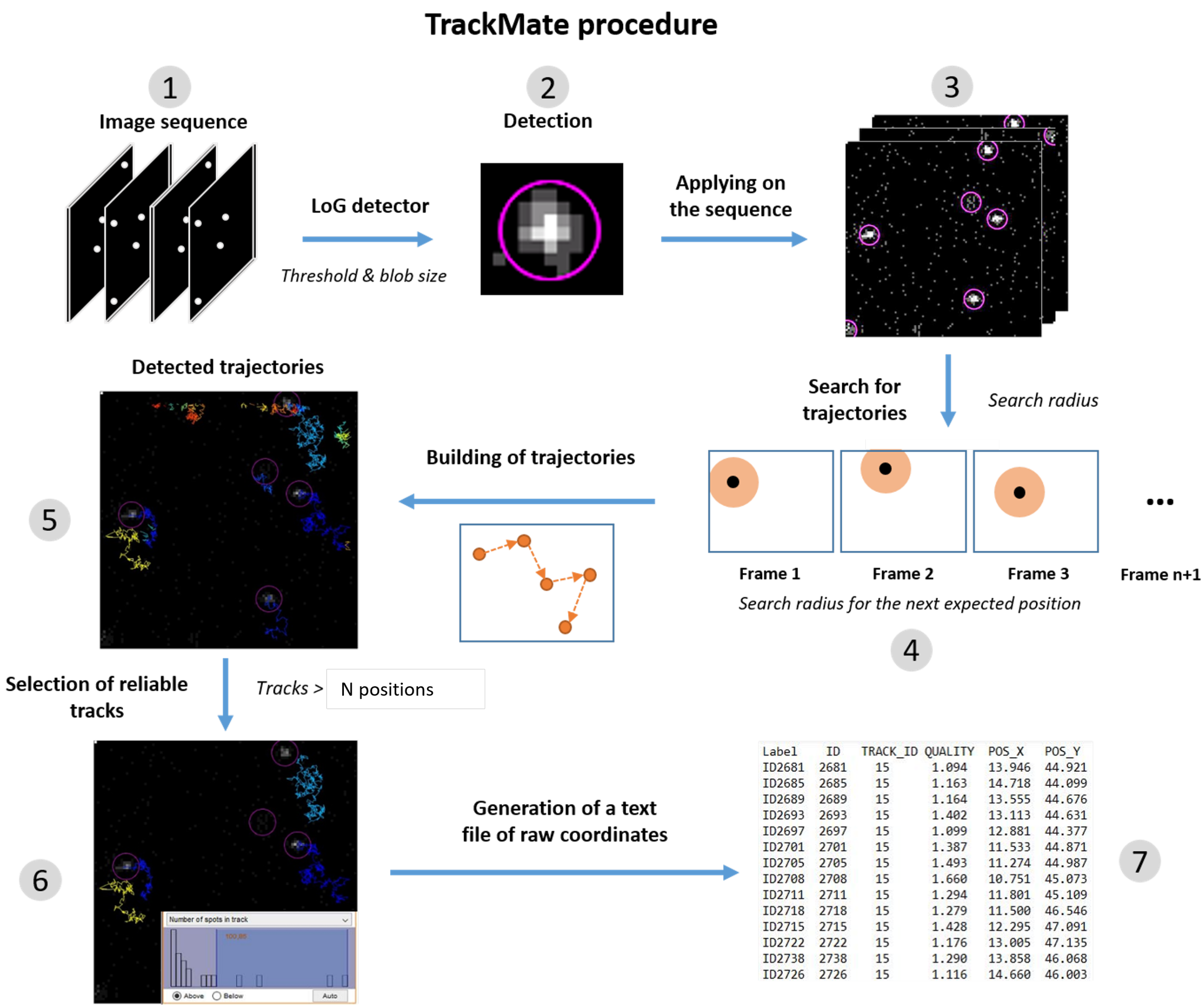

Figure 15 Flowchart of trackmate procedure used in this work.

12 Analyze of the track

12.1 Diffusion equation

It is possible to find the equation for diffusion simply using the mass conservation equation and Fick's first law.

Mass conservation mathematically translates the idea that if the amount of matter n has varied in a control volume V (which is written as $\iiint_V \partial n/\partial t$), it's because matter has entered or left through the boundaries, that is to say, the surface S of V. This can be written as $\oiint_S \boldsymbol{j} \cdot \boldsymbol{S}$, where $\boldsymbol{j} = n\boldsymbol{v}$ is the flux vector associated with the particle flow and $\boldsymbol{S} = S\boldsymbol{n}_S$, where n_S is a vector at every point perpendicular to the surface S and directed towards the outside. The mathematical transcription of mass conservation is then written as:

$$\iiint_V \frac{\partial n}{\partial t} = -\oiint_S \boldsymbol{j} \cdot \boldsymbol{S} \tag{26}$$

One can then make the volume V tend towards zero, and the flux across the surface becomes, almost by definition, equal to the divergence of the flux vector $\boldsymbol{j}$ (this is also known as the Green-Ostrogradsky theorem).

In the end, we get:

$$\frac{\partial n}{\partial t} + \operatorname{div} \boldsymbol{j} = 0 \tag{27}$$

where n is the particle concentration and $\boldsymbol{j} = n\boldsymbol{v}$ is the particle current density vector.

Fick's first law is described by:

$$\mathbf{j} = -D\nabla(n) \tag{28}$$

where D is the translational diffusion coefficient in $\mathrm{m\,s^{-2}}$. This law[6] mathematically translates that there exists a particle flux that tends to equalize concentrations within a sample. More precisely, a concentration inhomogeneity, which is mathematically translated by the concentration gradient, leads to the appearance of a particle flux ($\boldsymbol{j}$) in the direction where the concentration is the lowest (cf the minus sign).

Injecting Fick's law (equation 28) into the matter conservation equation 27 leads[7] to the diffusion equation:

$$\frac{\partial n}{\partial t} = D\Delta n \tag{29}$$

12.2 The jump probability

The jump probability is the probability for a particle to be at position r' after a given time knowing that it was at position r at $t = 0$. It directly derives from the diffusion equation.

Formulation The diffusion equation 29 can be rewritten in terms of the probability $P(x,t)$ of finding the particle at the abscissa x at time t. This probability also verifies the diffusion equation, which can be written in the 1D case as:

$$\frac{\partial P(x,t)}{\partial t} = D\frac{\partial^2 P}{\partial x^2} \tag{30}$$

[6] When it was stated in 1865 by Adolf Fick, it was an empirical law. It was later justified at the microscopic scale via statistical physics.
[7] The gradient of the divergence is equal to the Laplacian $\mathbf{grad}\,\mathrm{div} \leftrightarrow \Delta$

with the initial condition:

$$P(x,t=0) = u(x)$$

where $u(x)$ is any profile. In the case of a single particle found at $x=0$, $u(x) = \delta(x)$ where $\delta(x)$ is the Dirac distribution.

It is possible to solve the diffusion equation to know the jump probability using Fourier Transforms of the equation[8]. This leads, in the case of a point-like particle to the jump probability :

$$P_{\text{jump}}(\Delta x, \Delta t) = \frac{1}{\sqrt{4D\pi\Delta t}}, \exp\left(\frac{-(\Delta x)^2)}{4D\Delta t}\right) \tag{38}$$

where we have replaced x with the notation Δx and t with the notation Δt to indicate that these are differences between two values.

Properties of the jump probability

- The jump probability is a Gaussian with zero mean. Thus, the most probable position of a particle after a given time[9] is its starting position. On the other hand, the probability of the particle moving to the left ($x < 0$) is equal to that of moving to the right ($x > 0$).
- The second moment of the jump probability is its variance $Var = \sigma^2$ where σ is the standard deviation. We can directly identify it in the Gaussian of the jump probability and obtain:

$$\sigma^2 = 2D\Delta t \tag{39}$$

It is then possible to relate the variance σ^2 to the mean of the squared displacements $< (\Delta x)^2 >$ which we will subsequently denote as MSD (for Mean Squared Displacement). Indeed, via the

[8] To solve equation 30 we will apply a spatial Fourier transform, (The Fourier transform is indicated by the sign $\widehat{..}$), to both sides of the equation:

$$\frac{\delta \widehat{P(x,t)}}{\delta t} = Dfrac\delta^2 \widehat{\P(x,t)}\delta x^2 \tag{31}$$

The derivative property of a Fourier transform allows us to specify the spatial part of the equation (The variable k will indicate the spatial frequency) :

$$\frac{\delta^2 \widehat{P(x,t)}}{\delta x^2} = -4\pi^2 k^2 \hat{P}(x,t) \tag{32}$$

Since we apply a spatial Fourier transform, it will not affect the time derivative:

$$\frac{\delta \widehat{P(x,t)}}{\delta t} = \frac{\delta}{\delta t}\hat{P}(x,t) \tag{33}$$

The previous transformations, therefore, allow us to write:

$$\frac{\delta}{\delta t}\hat{P}(x,t) = -4D\pi^2 k^2 \hat{P}(x,t) \tag{34}$$

Which is a first-order linear differential equation whose solution is direct:

$$\hat{P}(x,t) = \hat{P}(x,t=0)\cdot e^{-4D\pi^2 k^2 t} \tag{35}$$

To obtain the jump probability of a particle, we need to apply the inverse Fourier transform ($\mathscr{F}^{-1}$), which will then transform the multiplication into a convolution product:

$$P(x,t) = P(x,t=0) * \mathscr{F}^{-1}[e^{-4D\pi^2 k^2 t}] \tag{36}$$

We have as initial condition $P(x,t=0) = \delta(x)$ since we have a unique particle that is therefore perfectly localized at time $t=0$, the inverse Fourier transform of a Gaussian is calculated simply since the inverse transform keeps the Gaussian form. We then obtain:

$$P(x,t) = \delta(x) * \left(\frac{1}{\sqrt{4D\pi t}}\cdot \exp[\frac{-x^2}{4Dt}]\right) \tag{37}$$

As previously said, a particle is considered as point-like, so it is the impulsive response of the diffusive system. In this sense, the jump probability (eq.38) is the Green's function of the system. The analytical jump probability for a one-dimensional particle is therefore simply expressed by a Gaussian.

[9] Any time actually, as the probability is time-invariant.

Konig-Huygen theorem[10]

$$\sigma^2 = < (\Delta x)^2 > - (< \Delta x >)^2 = < (\Delta x)^2 > \tag{40}$$

since the probability has a zero mean $< \Delta x >$.

In the end, and this is a crucial point for what follows, we can relate the diffusion coefficient D of a particle to its MSD:

$$< (\Delta x)^2 > = 2D\Delta t \tag{41}$$

We define a typical Brownian motion length L_{brown} which corresponds to the average distance[11] covered in a given direction by a particle during the time Δt such as:

$$L_{\text{brown}} = \sqrt{2D\Delta t} \tag{42}$$

This characteristic distance plays a very important role when we want to examine the order of magnitude of the importance of Brownian motion compared to other phenomena that may occur experimentally.

Thus, unlike translational motion, the distance covered by a particle via Brownian motion is not proportional to time ($x \neq vt$) but proportional to the *square root* of time.

- The jump probability, and the associated Brownian motion, *has no memory.* In more mathematical terms, there is, theoretically, no correlation between the Brownian jump that occurs between 0 and Δt and the one between Δt and $2\Delta t$. By indexing the first Brownian jump by n and the next by $n+1$ we then have mathematically[12]:

$$< \Delta x_n \Delta x_{n+1} > = 0 \tag{43}$$

In other words, the covariance of two successive jumps is zero.

12.3 Accounting for Convective Motion

Even for small particles, Brownian motion remains relatively weak compared to potential residual convection movements within the fluid.
This is especially true in our case in our studies within microfluidic chips made of silicone. Indeed, this material is relatively flexible and its deformation is comparable to the role of a capacitor in an electrical setup. Just as there is a relaxation time $\tau = RC$ for the current i in an electrical circuit, the equivalent exists in a microfluidic circuit. The flow, and the associated convection motion, definitively stop only after a relaxation time. On the other hand, any difference in liquid level within the microfluidic setup leads to a hydrostatic pressure that can give rise to a non-zero residual flow.

[10] Let's denote the average of a quantity x by $< x >$. The variance is by definition the moment of order 2 given by:

$$\sigma^2 = < (x - < x >)^2 >$$

or in other words, the mean of the squared deviations from the mean. So:

$$\sigma^2 = < x^2 - 2x < x > + (< x >)^2 >$$

Since the mean is distributive and with $<< x >> = < x >$, we can write:

$$\sigma^2 = < x^2 > - 2 < x >< x > + (< x >)^2)$$

to finally obtain:

$$\sigma^2 = < x^2 > - (< x >)^2$$

[11] This may seem paradoxical as this distance is not zero, as indicated earlier, the average displacement $< \Delta x >$ is zero...

[12] The mean value of the product of two Gaussians centered at zero also has a mean value of zero.

In the presence of a global convective motion at speed v, the Brownian jump probability (eq. 38) is modified to become [6]:

$$P_{\text{jump, drift}}(\Delta x, \Delta t) = \frac{1}{\sqrt{4D\pi\Delta t}} \exp\left(\frac{-(\Delta x - V\Delta t)^2}{4D\Delta t}\right) \tag{44}$$

The presence of a drift leads to this new jump probability, which in turn modifies the characteristics of the motion:

- The average value of the displacements $< \Delta x >$ is no longer zero. It is now $< \Delta x >= V\Delta t$, i.e., the displacement due to the drift at speed V during time Δt.
- The variance of the jump probability remains the same, namely $\sigma^2 = 2D\Delta t$ but the application of the Huygens-Kronig theorem now must involve a non-zero average $< \Delta x >$ so that:

  $$\sigma^2 = 2D\Delta t =< (\Delta x)^2 > -(< \Delta x >)^2 =< (\Delta x)^2 > -(V\Delta t)^2 \tag{45}$$

  and we therefore obtain for the MSD $< (\Delta x)^2 >$:

  $$< (\Delta x)^2 >= 2D\Delta t + (V\Delta t)^2 \tag{46}$$

  In the presence of drift, the MSD is no longer proportional to time Δt and has an additional quadratic term due to the drift. Even if the speed V of this drift leads to a convection movement that is weak compared to the amplitude of the Brownian motion ($V\Delta t \leq \sqrt{2D\Delta t}$), its intervention at power 2 in the expression of the MSD means that it will eventually dominate in the long term.
- Convection motion does not create a memory effect and two successive jumps still have no correlation. Indeed, a generalization of the Huygens-Konig theorem allows to write the covariance $\text{Cov}(x,y)$ of two random variables x and y from the expression of their mean.

  $$\text{Cov}(x,y) =< P(x)P(y) > - < P(x) >< P(y) > \tag{47}$$

  where $P(x)$ and $P(y)$ are respectively the probability law of x and y which are here the jump probability of eq.44. Consequently, with a speed V for the drift, the covariance noted here

  $$\text{Cov}(x,y) = ((V\Delta t) \times (V\Delta t)) - (V\Delta t)(V\Delta t) = 0 \tag{48}$$

12.4 Accounting for Experimental Uncertainties

While theoretically, Brownian motion is memoryless, the consecutive displacements of a particle in an experimental measurement are actually correlated. Mathematically:

$$< \Delta x_n \Delta x_{n+1} >=< (x_n - x_{n-1})(x_{n+1} - x_n) >\neq 0 \tag{49}$$

The key point is that both displacements share the n-th frame of the film. If there is experimental uncertainty at the n-th frame, this will artificially couple the n and n+1 displacements, making the covariance $< \Delta x_n \Delta x_{n+1} >$ non-zero.

These uncertainties have two origins :

- The error termed as *static error* originates from the noise (background noise or even shot noise) that is a natural part of any experiment involving particle tracking.
- *Dynamic error* is a result of the time needed for acquiring position measurements, often referred to as shutter time.

  Additionally, it is important to note that during the image acquisition period, the particle continues to exhibit Brownian motion. Contrary to the motion blur typically observed in convective flow, which manifests as a trailing streak, the particle's movement in this context results in a diffusive halo surrounding its position.

The community has acknowledged that static localization noise, which is the random deviation in determining the position of a stationary particle, impacts the Mean Square Displacement (MSD) with [7]:

$$< (\Delta x_n)^2 >= 2D\Delta t + 2\sigma^2$$

In this context, σ represents the static localization error, which is the standard deviation of the measured positions for a particle that is not in motion (deposited on a coverslip for instance).

As for the dynamic error, the MSD is modified as :

$$< (\Delta x_n)^2 >= 2D\Delta t - 4DR\Delta t \quad , \quad 0 \leq R \leq 1/4$$

where R is the "motion blur coefficient", describes the pattern of light exposure, or alternatively the condition of the camera's shutter, throughout the camera's period of image capture [8]. In the most common case, that is to say full-frame averaging, $R = 1/6$.

In total, in the case of $R = 1/6$, we have :

$$< (\Delta x_n)^2 >= 2D\Delta t + \underbrace{2\sigma^2}_{\text{static}} - \underbrace{\frac{2}{3}DR\Delta t}_{\text{dynamic}}$$

This gives rise to two observations :

- This is a substantial correction from the very frequently used unmodified MSD approach. Taking into account the dynamic error decreases the coefficient diffusion by 33%.
- As said in the introduction of this section, while a Brownian particle in free motion has displacements that are not correlated, motion blur and static localization noise create correlations in the displacements that are actually observed.

  The localization errors, represented by σ, lead to a *negative* correlation. This can be comprehended by recognizing that both $\Delta_{k-1} = x_k - x_{k-1}$ and $\Delta_k = x_{k+1} - x_k$ are influenced by the same noise value at frame k, but with opposing signs.

  Motion blur, on the other hand, gives rise to a *positive* correlation. This is a well-known effect that is akin to a *low-pass filter* being applied to the inherent motion when averaging across frames.

The static localization error σ can be obtained experimentally or calculated via the covariance of the time series of the displacement Δx :

$$\sigma = R < (\Delta x_n)^2 > +(2R - 1) < \Delta x_n \Delta x_{n+1} > \tag{50}$$

In the present study, the amendments introduced by accounting for the localization error denoted as σ, were relatively minor, on the order of a few percents. However, it was observed that σ exhibited significant variations between individual tracks, solely attributable to statistical fluctuations. This is not compatible with the experimental conditions, where the Signal-to-Noise Ratio (SNR) remained almost constant across the measurement plane. Consequently, it would be more methodologically sound to establish a fixed experimental value for σ, if feasible.

12.5 Drift correction

A first correction can be made only with the data from one track. A pure Brownian motion should have a zero mean displacement $< \Delta x >= 0$. If it not the case, it can be attributed to a residual drift. A very simple correction for the drift is then to subtract all displacements in one track from the mean value of these displacements. This approach is simple to implement but has two limitations. Firstly, it assumes that the drift is constant during all the tracks and secondly, even with no drift at all, the mean of displacements can be different from zero due to statistical fluctuations. More precisely, if a track contains N points, the confidence interval on the estimation of the mean $< \Delta x >_{\text{estimate}}$ from only those N points is given by the standard error of the mean (SEM) :

$$< \Delta x >_{\text{estimate}} = < \Delta x >_{\text{true}} \frac{s}{\sqrt{N}} \tag{51}$$

Here, s is the sample standard deviation of the displacement values, and N is the number of points in the track.

The following two techniques[9] are capable of determining drift solely based on the trajectories of the particles, provided that there are enough particles and that they are adequately sampled.

The first one, the centroid method, calculates the mean position of all particles at every moment in time and considers this average position as representative of the drift. The speed of the centroid position is taken as the drift. This method is prone to error and needs a large number of particles to have a correct estimate of a reliable centroid.

The subsequent approach, the drift correction using velocity correlation, addresses these issues by employing a straightforward observation. Given that we're dealing with a uniform drift, the displacement attributable to the drift will be consistent across all particles at any specific time. In addition to this shared displacement, each individual particle will experience a separate displacement due to Brownian motion, which is what we aim to measure. To put this into mathematical terms, the velocity of the i-th particle can be represented as follows :

$$\boldsymbol{v}_i(t) = \boldsymbol{v}_{\text{drift}}(t) + \boldsymbol{v}_{\text{diffusive}}(t)$$

Now, if we consider the mean velocity $< \boldsymbol{v}(t) >$ of all the particles :

$$< \boldsymbol{v}(t) > = \sum_i (\boldsymbol{v}_{\text{drift}}(t) + \boldsymbol{v}_{\text{diffusive}}(t))$$

However, the diffusive motions of individual particles are independent of each other. Given a sufficiently large number of particles, it's reasonable to expect that the second term in the sum will effectively cancel out to zero. As the first term in the sum is not influenced by the variable i, we can express it as follows :

$$\boldsymbol{v}_{\text{drift}}(t) = < \boldsymbol{v}(t) > \tag{52}$$

12.6 Software implementation

A home-made software[13] was developed in Python in order to analyze the raw track data obtained from TrackMate.

[13] `https://github.com/MLoum/pyAnalyzeTrack`. At the time of writing, the code is functional but needs a lot of cleaning and commenting.

13 Effect of the roughness of the PDMS wall on the light sheet

Figure 16 presents the effect of the roughness of the PDMS wall on the light sheet *lateral* profile, that is to say, the one that is imaged on the camera and where the cylindrical lens has no focalization effect, calculated using diffractio for different roughness parameters. More precisely, a correlation length of $t = 20\mu$m for the roughness of the wall was chosen in accordance with the pixel size of the LCD used for the photolithography of the master mold for the microfluidics chip. The standard deviation s of the roughness is changed across the different graphs in Fig. 16.

The numerical simulations show similar tendencies to the experimental images, that is to say, the apparition of what can be described as rays of light that reduces the intensity homogeneity of the light sheet. In the case where the Gaussian only crosses one rough PDMS wall, the other one being smooth out by the contact of the cylindrical lens, and that the rough PDMS wall is in contact with water, the fringes in the light sheet only appear for $s = 1\,\mu$m.

Figure 17 presents the effect of the roughness of the PDMS wall on the light sheet axial (i.e. z profile) calculated using diffractio for different roughness parameters. Abberation on the light sheet profile can be spotted starting at $s = 500$nm and from $s = 5\mu$m the profile is compromised.

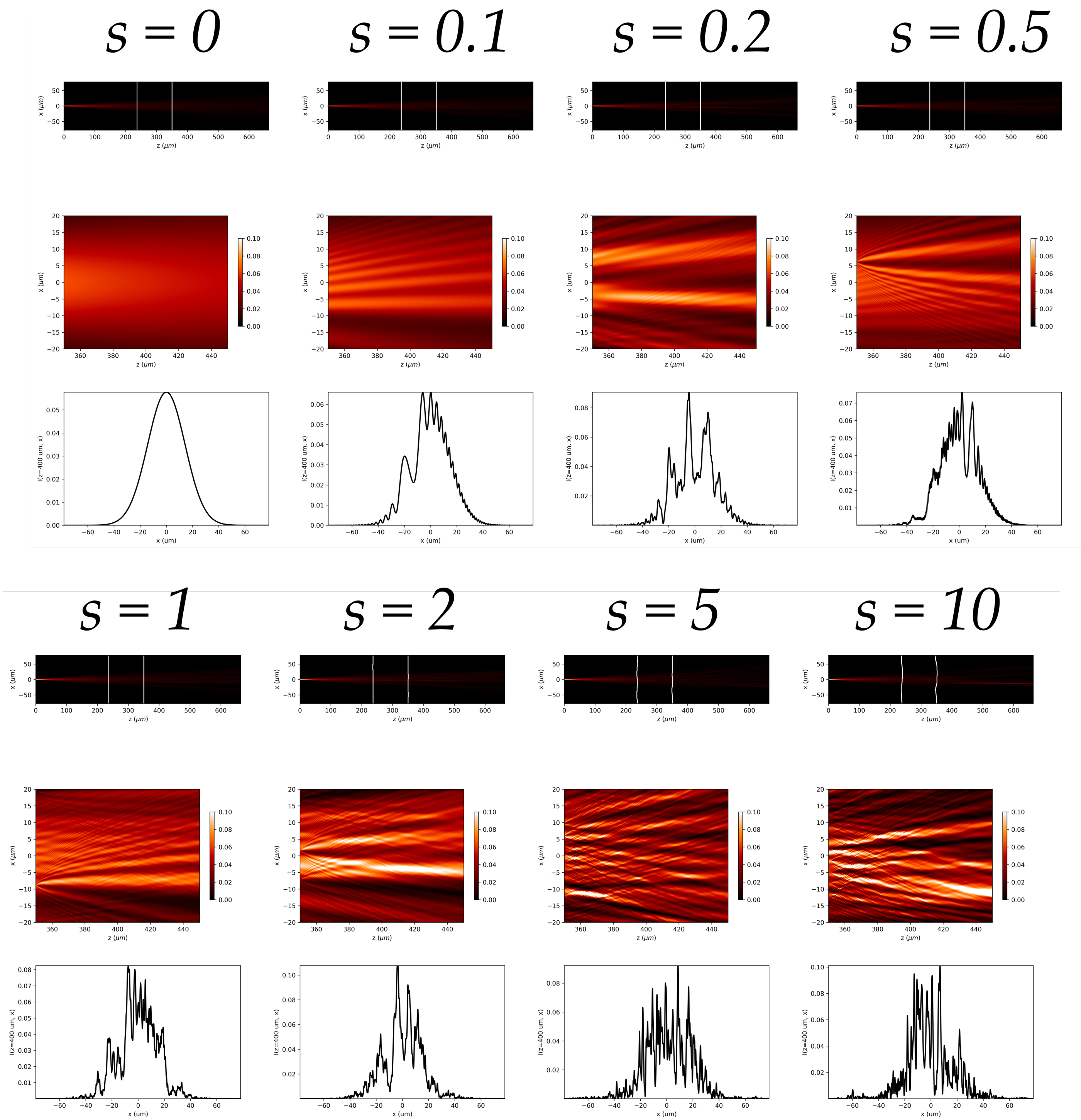

Figure 16 Effect of the roughness on the lateral profile (i.e. the one not affected by the cylindrical lens) for different values s of the standard deviation of the roughness. The correlation length of the roughness was set at $t = 20\mu\mathrm{m}$. The index of refraction is 1.44 in the PDMS and 1 everywhere else.

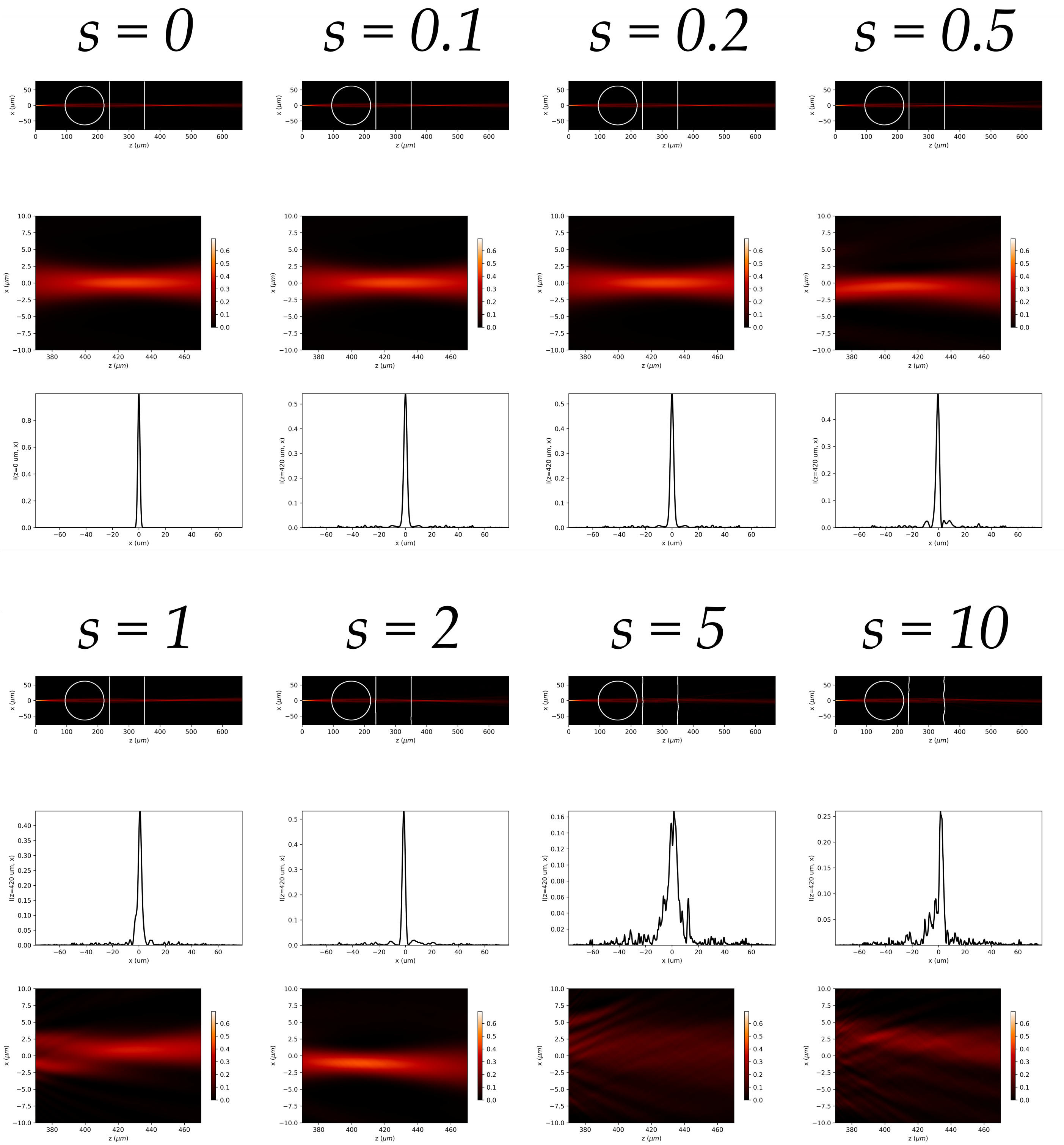

Figure 17 Effect of the roughness on the axial profile (i.e. along the optical axis) for different values s of the standard deviation of the roughness. The correlation length of the roughness was set at $t = 20\mu\text{m}$. The index of refraction is 1.44 in the PDMS and 1 everywhere else.

14 Trapezoidal shape of the microchannel

The beam of UV light used to illuminate the dry film photoresist is not well collimated. Consequently, the walls of the master mold are slightly inclined and this angle is transferred to the PDMS chip. This effect can be quantified by imaging a channel on the master mold by its side. The images obtained with a stereo microscope binoculars are shown in figure 18

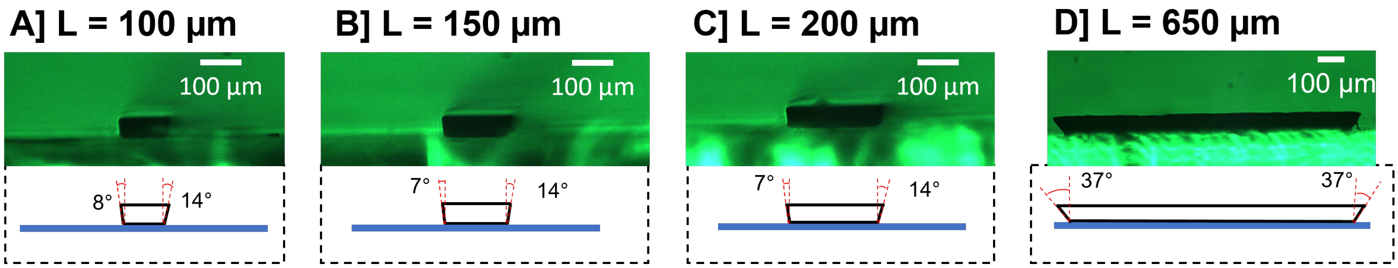

Figure 18 Images of the master mold imaged on the sides obtained with stereo microscope binoculars. From the picture, the angle of the wall can be estimated at around 10°.

15 NTA movies

NTA videos are in Audio Video Interleave (AVI) format with MJPEG video codec. They are stored on the University of Angers cloud.

link 1: https://uabox.univ-angers.fr/index.php/s/k3TXIPu2kLqUPkZ

Filename : x20_60fps_50nm_or_C0sur_1000_frames.avi

Movie used to analyze individual particle tracking (NTA) of 50 nm gold nanoparticles. 1000 frames, frame rate: 60 fps, duration: 16.6 seconds.

link 2: https://uabox.univ-angers.fr/index.php/sMczfngNYtYxyQ2I

Filename : x20_60fps_80nm_or_C0sur_1000_frames.avi

Movie used to analyze individual particle tracking (NTA) of 80 nm gold nanoparticles. 1000 frames, frame rate: 60 fps, duration: 16.6 seconds.

Notes and references

[1] L. M. Sanchez Brea. diffractio: Python module for diffraction and interference optics. `https://pypi.org/project/diffractio/`, 2019.

[2] E. Hecht. *Optics*. Pearson, 2012.

[3] A. Gerrard and J.M. Burch. *Introduction to Matrix Methods in Optics*. Dover Books on Physics. Dover, 1994.

[4] EPFL. Psf generator, 2023. Accessed: 2023-02-15.

[5] Théo Travers, Vincent G. Colin, Matthieu Loumaigne, Régis Barillé, and Denis Gindre. Single-particle tracking with scanning non-linear microscopy. *Nanomaterials*, 10(8):1519, 2020.

[6] S. Chandrasekhar. Stochastic problems in physics and astronomy. *Rev. Mod. Phys.*, 15:1–89, Jan 1943.

[7] Norman Bobroff. Position measurement with a resolution and noise-limited instrument. *Review of Scientific Instruments*, 57(6):1152–1157, 06 1986.

[8] Andrew J. Berglund. Statistics of camera-based single-particle tracking. *Phys. Rev. E*, 82(1):1–8, 2010.

[9] Jean-Yves Tinevez. Mean square displacement analysis: Drift correction, 2023. Accessed on February 1, 2023.